Chapter 6
Extraction of Copper Oxide (II): Copper Oxide Nanoparticles

Daniel Ogochukwu Okanigbe (ORCID)

6.1 Introduction

The available resource recovery processes have capital and operating expenses that are higher than what the revenue from the recovered metal can support. In order to recover the copper value from metallurgical wastes such as copper anode slimes, copper slags, waste copper dust (WCD), the copper smelting industry is becoming more and more interested in inventing ways for doing so. It would be advantageous to have a processing technique that could eliminate impurities from the WCD while maintaining a suitable level of revenue metals in the resultant concentrate.

To facilitate the management of accumulated WCD, it would be desirable if this could be done economically. It is believed that recovering copper as oxides of nanoparticles (CuO-NPs) from purified pregnant leach solution (PPLS) is preferable to recovering it as cathode slabs [1]. This is because CuO-NPs outperform conventional copper oxide in many applications thanks to their exceptional physicochemical characteristics. Recently, there has been increased interest in producing CuO-NPs with p-type semiconductivity [2]. CuO-NPs are recognized as one of the best inorganic semiconductors with desirable properties [3].

Moreover, CuO-NPs can be used in a wide range of technological applications, such as gas sensors [4, 5], magnetic phase transmitters [6], heterogeneous catalysts [7–9], and optical switches [6, 10, 11], nanofluids [12, 13], solar energy transformer [4, 14], lithium ion electrode materials [8, 15], and field emitter [6, 11].

Due to the vast range of uses for metallic/metallic oxide nanoparticles, numerous methods for manufacturing them via chemical, physical, and biological processes

D. O. Okanigbe (✉)
Department of Chemical, Metallurgical and Materials Engineering, Faculty of Engineering and the Built Environment, Tshwane University of Technology, Pretoria, South Africa

Pantheon Virtual Engineering Solutions, Nigel, South Africa
e-mail: okanigbedo@tut.ac.za; okanigbeogochukwu@gmail.com

have also been documented (CuO-NPs). Sol-gel [16], wet chemical approaches [17, 18], thermal oxidation of Cu substrates [10], and solvothermal methods [4, 6], microwave irradiation [19], sonochemical [20], and microemulsion [21], electro-chemical [22], hydrothermal [23, 24], solid-state reaction [25, 26], submerged arc [27], and precipitation methods [12, 28, 29] are a few examples of these techniques. Co-precipitation and the thermal degradation of precursors are additional methods for producing nanoparticles [28, 30–32].

A key consideration in selecting the best technique is how to generate copper or copper oxide nanoparticles with an acceptable level of purity [27]. In a closed vessel, such as an autoclave, solvents are heated significantly above their boiling temperatures in a solvothermal process that involves chemical interaction. When water is used as the solvent, the process is referred to as a hydrothermal one. A variety of literatures have discussed how this strategy is used [33, 34]. Byrappa and Yoshimura [35] described the hydrothermal process as a process involving a heterogeneous chemical reaction in a closed system, in the presence of an aqueous or non-aqueous solvent above room temperature, and at pressures more than 1 atm.

When water is 647.15 K and 221 bar above atmospheric pressure, it is referred to as a supercritical fluid. Water or other fluids that are supercritical behave both like liquids and like gases. Surface tension is decreased when a solid and a supercritical fluid come into contact, and chemical compounds that are extremely difficult to dissolve in ambient conditions are also dissolved. These techniques largely take use of the metal's higher solubility and reactivity [36]. There are many advantages to using supercritical conditions, including simplicity, very small grain size, the presence of a single phase, and the creation of high-purity nanocrystals with outstanding crystallinity and green properties [37].

The thermal reduction technique is an illustration of a solvothermal process. This technology exceeds older ones like the chemical reduction method in terms of cleanliness, speed, and cost despite being relatively new. It requires the appropriate precursor to be picked, as well as focused heating. Numerous studies have shown that this method can produce copper oxide nanoparticles. According to Zhang et al. [8], the thermal breakdown of the copper oxalate precursor produced CuO-NPs with an average diameter of 10 nm. CuO nanoparticles were also produced from the thermal breakdown of the precursors brochantite $Cu_4(SO_4)(OH)_6$ and posnjakite $Cu_4(SO_4)(OH)_6.H_2O$ [38]. Simpleness, a high possibility of single-phase, high-purity nanocrystals with high crystallinity, low particle size, and favourable environmental effects are all guaranteed by this method [27, 37].

A few studies have been done on the production of CuO-NPs by the thermal breakdown of copper precursors in a CSD's leach solution [27, 32, 38]. Additionally, the thermal decomposition method for creating CuO-NPs from CSD requires careful selection of a copper precursor, as was previously mentioned in the preceding paragraphs [27]. Therefore, it is essential to optimize the process parameters of agitation speed, temperature, flow rate, and concentration of both Na_2CO_3 and $CuSO_4$ in order to obtain the best copper precursor, which will support the production of CuO-NPs with enhanced grade and recovery during its thermal decomposition.

Thus, this chapter presents the results of the inquiry into the production of CuO-NPs from this low-grade waste metal dust (i.e. CSD).

6.2   Experimental Method

6.2.1   Material

6.2.1.1   Waste Metal Dust

The WCD from South Africa served as the waste metal dust in this investigation.

6.2.2   Methods

6.2.2.1   Production of Pregnant Leach Solution (PPLS)

In Okanigbe [39], the method for creating the PPLS employed in the synthesis of the CuO-NPs is described.

6.2.2.2   Design of Experiment and Procedure for Production of Copper Precursor

Starting with the manufacture of copper precursor from PPLS, CuO-NP manufacturing began. The 3-by-2 complete factorial experimental design approach was used to create the experiment design for the manufacture of copper precursor from PPLS, as illustrated in Tables 6.1 and 6.2.

The copper precursor was made by adding 2 M Na_2CO_3 solution dropwise to 0.2 M $CuSO_4$ solution in a 500-ml conical flask that was set on a hot plate while the mixture was stirred with a magnetic stirrer at various temperatures (Fig. 6.1). Filtration was used to separate the resultant green precipitate, which was then washed with distilled water and pure ethanol. Then, for 24 h, this green precipitate is dried in an oven at 105 °C.

Table 6.1 Parameters considered for the production of copper precursor

	Levels		
Parameters	Low	Medium	High
Temperature (°C)	25	55	85
Rotational speed (rpm)	340	740	1480

Table 6.2 Design of experiment for the production of copper precursor

Tests	Temperature (°C)	Rotational speed (rpm)	Treatment combinations (TC)
1	25	340	25 °C/340 rpm
2	25	740	25 °C/740 rpm
3	25	1480	25 °C/1480 rpm
4	55	340	55 °C/340 rpm
5	55	740	55 °C/740 rpm
6	55	1480	55 °C/1480 rpm
7	85	340	85 °C/340 rpm
8	85	740	85 °C/740 rpm
9	85	1480	85 °C/1480 rpm
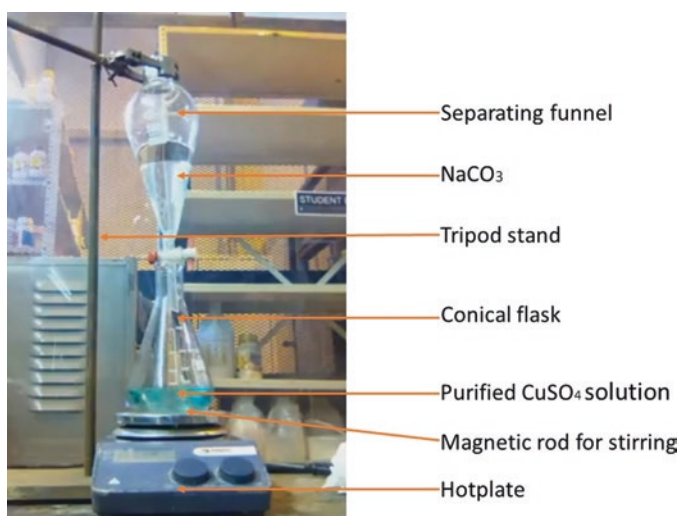
Fig. 6.1 Experimental setup for the production of copper precursor

6.2.2.3 Design of Experiment and Procedure for Production of CuO-NPs from Copper Precursor

Using a thermogravimetric analyser and an atmospheric flow, it was determined how the synthetized copper precursor behaved thermally. Thirty-five milligrams of samples was placed in a platinum crucible on the microbalance pan and heated between 25 and 1000 °C at rates of 5, 10, 15, and 20 °C/min.

The 3-by-2 complete factorial experimental design method was used to create the study (Tables 6.1 and 6.2). Soon after becoming familiar with the copper precursor's thermal behaviour, the experiment was planned using the data, as can be seen in Tables 6.3 and 6.4 for the production of CuO-NPs. Experimental procedure can be found in Okanigbe [39].

Table 6.3 Parameters considered for the production of CuO-NPs

Parameters	Levels		
	Low	Medium	High
Temperature (°C)	650	750	850
Time (h)	1	2	3

Table 6.4 Design of experiment for production of copper nanoparticles

Tests	Temperature (°C)	Time (h)	TC
1	650	1	650 °C/1 h
2	650	2	650 °C/2 h
3	650	3	650 °C/3 h
4	750	1	750 °C/1 h
5	750	2	750 °C/2 h
6	750	3	750 °C/3 h
7	850	1	850 °C/1 h
8	850	2	850 °C/2 h
9	850	3	850 °C/3 h

6.3 Results and Discussion

6.3.1 Mineralogy of Copper Precursor

This investigation into the synthesis of CuO-NPs from low-grade waste metal dust PPLS from South African CSD focuses on the synthesis and characterization of copper precursors before thermally decomposing the copper precursors to produce CuO-NPs. The many physical and chemical techniques used for material characterization are summarized in this section. Various physical characterization techniques, including powder X-ray diffraction, SEM, and TEM, were used to evaluate the copper precursor and CuO-NPs samples that were produced.

According to published literatures [27, 32, 40, 41], the thermal dehydration and desulpheration processes (Eqs. 6.1–6.3) are part of the reaction pathway that leads to copper (II) oxide. Equations 6.1–6.3 demonstrate that the three separate steps of the decomposition of $CuSO_4$ in solution were dehydration (Eq. 6.1), crystallization (Eq. 6.2), and desulphurization (Eq. 6.3) according to Koga et al. [41].

$$Cu_4(SO_4)(OH)_6 \cdot xH_2O \xrightarrow{170-180°C} CuSO_4 \cdot 3Cu(OH)_2 + xH_2O \tag{6.1}$$

$$CuSO_4 \cdot 3Cu(OH)_2 \xrightarrow{170-180°C} CuSO_4 \cdot 2Cu(OH)_2 + CuO + xH_2O \tag{6.2}$$

$$CuSO_4 \cdot 2Cu(OH)_2 \xrightarrow{170-180°C} CuO + xH_2O + SO_2 + \frac{1}{2}H_2O \tag{6.3}$$
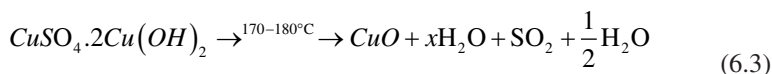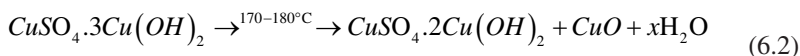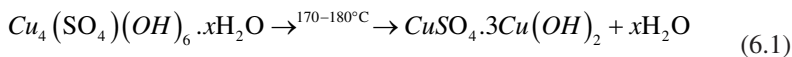
6.3.1.1 Mineralogy of Copper Precursor Produced Under TC 25 °C/340 rpm

The XRD machine was used to characterize the crystal structure and phase purity of the copper precursor generated under TC of 25 °C/340 rpm (Table 6.2). Figure 6.2 demonstrates that exactly 87.1% of all the diffraction peaks were indexed to hydrotalcite, while 4.8% of the peaks were indexed to aragonite, and the remaining 8.2% of the peaks were indexed to the copper-containing compounds 0.1% posnjakite and 8.1% cuprite.

6.3.1.2 Mineralogy of Copper Precursor Produced Under TC 25 °C/740 rpm

Figure 6.3 displays the crystal structure and phase purity of the copper precursor produced at TC of 25 °C/740 rpm (Table 6.2). The majority of the diffraction peaks, 82.9%, were attributed to hydrotalcite, while 5.0% is indexed to aragonite. The remaining 0.1% and 12.1% of the peaks were attributed to the copper-containing minerals posnjakite and cuprite, respectively.

6.3.1.3 Mineralogy of Copper Precursor Produced Under TC 25 °C/1480 rpm

XRD was used to characterize the crystal structure and phase purity of the copper precursor generated under TC of 25 °C/340 rpm (Table 6.2). As can be seen in Fig. 6.4, hydrotalcite accounted for exactly 86.5% of all the diffraction peaks, while
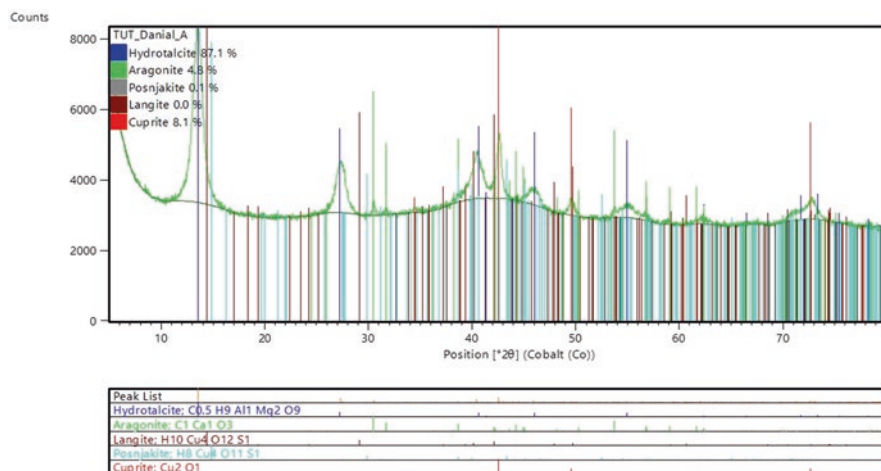

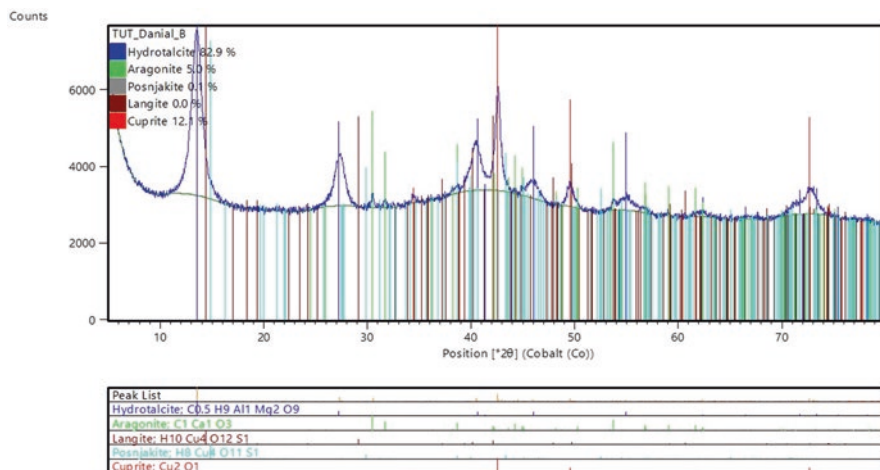**Fig. 6.2** XRD result of copper precursor obtained under 25 °C/340 rpm TC

Fig. 6.3 XRD result of copper precursor obtained under 25 °C/740 rpm TC
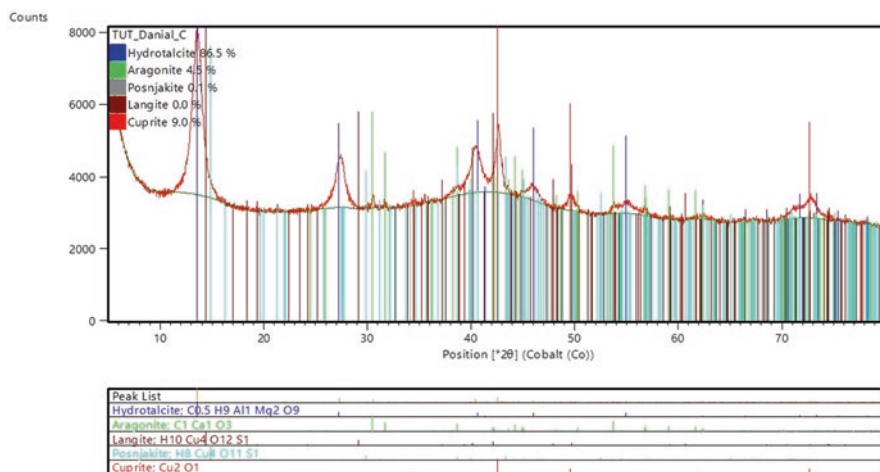

Fig. 6.4 XRD result of copper precursor obtained under 25 °C/1480 rpm

4.5% of them were indexed to aragonite, the other diffraction peaks were indexed to posnjakite (0.1%) and cuprite (9.0%).

6.3.1.4 Mineralogy of Copper Precursor Produced Under TC 55 °C/340 rpm

By using the XRD, the crystal structure and phase purity of the copper precursor produced at TC of 55 °C/340 rpm (Table 6.2) were identified. According to Fig. 6.5, the exact percentage of diffraction peaks indexed to hydrotalcite was 92.3%, the percentage indexed to aragonite was 2.7%, and the percentage indexed to cuprite was 5.1%.

6.3.1.5 Mineralogy of Copper Precursor Produced Under TC 55 °C/740 rpm

XRD was used to characterize the crystal structure and phase purity of the copper precursor generated under TC of 55 °C/740 rpm (Table 6.2). Figure 6.6 demonstrates that exactly 88.1% of all the diffraction peaks were indexed to hydrotalcite, while 3.0% of the peaks were indexed to aragonite, and the remaining 0.1% and 8.8% of the peaks were indexed to cuprite.

6.3.1.6 Mineralogy of Copper Precursor Produced Under TC 55 °C/1480 rpm

XRD was used to characterize the crystal structure and phase purity of the copper precursor generated under TC of 55 °C/1480 rpm (Table 6.2). As can be seen in Fig. 6.7, hydrotalcite accounted for exactly 89.5% of all the diffraction peaks, while 2.6% of them were indexed to aragonite, the other diffraction peaks were indexed to
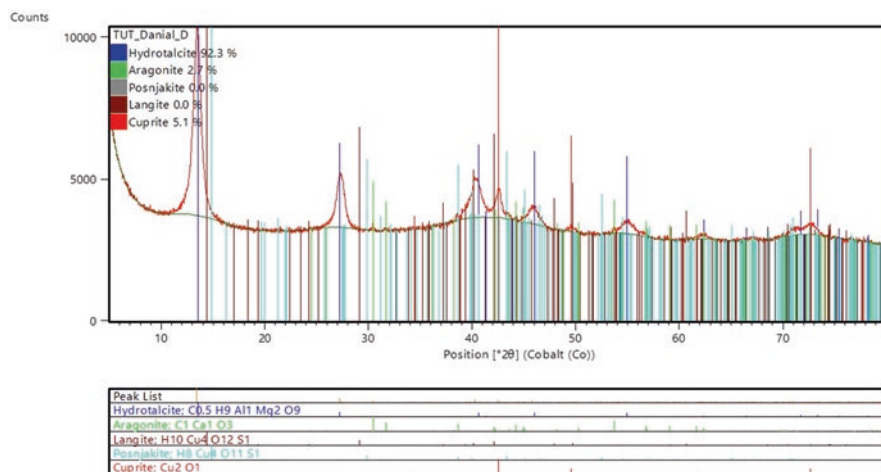

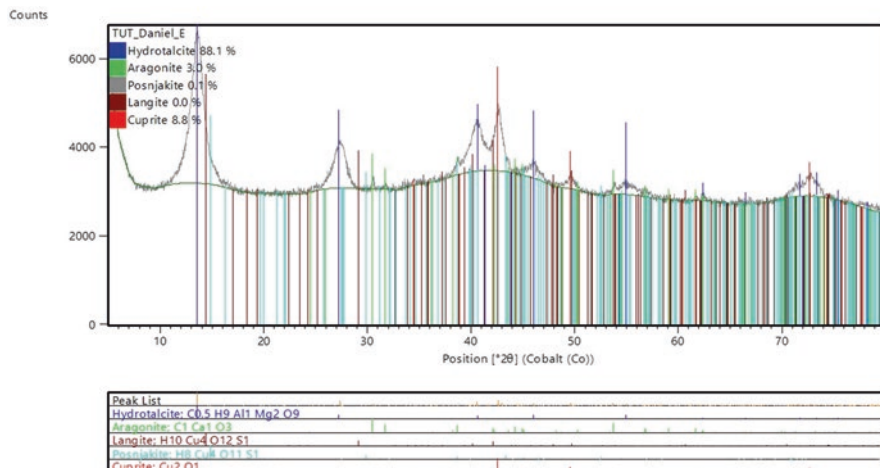**Fig. 6.5** XRD result of copper precursor obtained under 55 °C/340 rpm

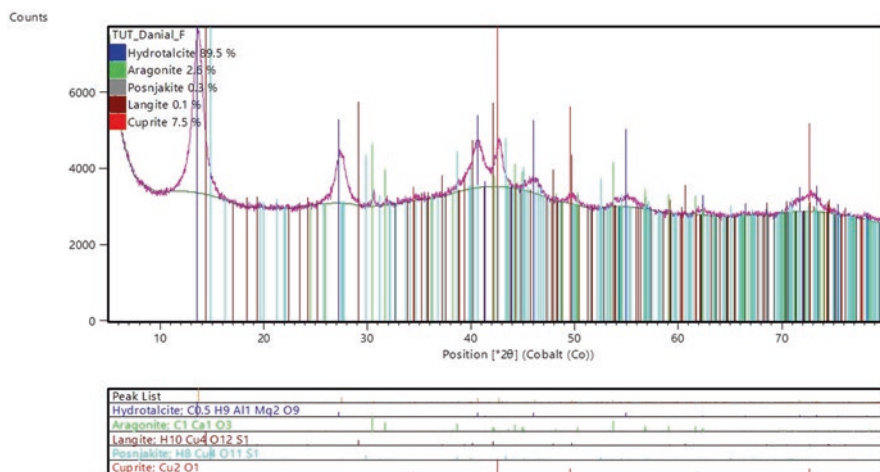**Fig. 6.6**   XRD result of copper precursor obtained under 55 °C/740 rpm

Fig. 6.7   XRD result of copper precursor obtained under 55 °C/1480 rpm

the copper-containing compounds posnjakite (0.3%), langite (0.1%), and cuprite (7.5%).

6.3.1.7 Mineralogy of Copper Precursor Produced Under TC 85 °C/340 rpm

The copper precursor produced at TC 85 °C/340 rpm (Table 6.2) was examined using the XRD apparatus for its crystal structure and phase purity. According to Fig. 6.8, precisely 68.3% of all the diffraction peaks were indexed to hydrotalcite, 11.0% to aragonite, and the remaining peaks were indexed to posnjakite (4.8%) and cuprite (15.9%).

6.3.1.8 Mineralogy of Copper Precursor Produced Under TC 85 °C/740 rpm

The XRD machine was used to characterize the crystal structure and phase purity of the copper precursor generated under TC of 85 °C/740 rpm (Table 6.2). Figure 6.9 reveals that exactly 83.2% of all the diffraction peaks were indexed to hydrotalcite, while 3.5% of the peaks were indexed to aragonite, and the remaining 13.3% of the peaks were indexed to posnjakite (0.1%) and cuprite (13.2%).

6.3.1.9 Mineralogy of Copper Precursor Produced Under TC 85 °C/1480 rpm

The crystal structure and phase purity of the copper precursor produced at TC of 85 °C/1480 rpm (Table 6.2) are shown in Fig. 6.10. 70.3% of the diffraction peaks were attributable to hydrotalcite, whereas aragonite was responsible for 10.6% of the peaks. Posnjakite, langite, and cuprite are the copper-containing minerals that are responsible for the remaining diffraction peaks, 5.8%, 1.6%, and 11.7%, respectively.
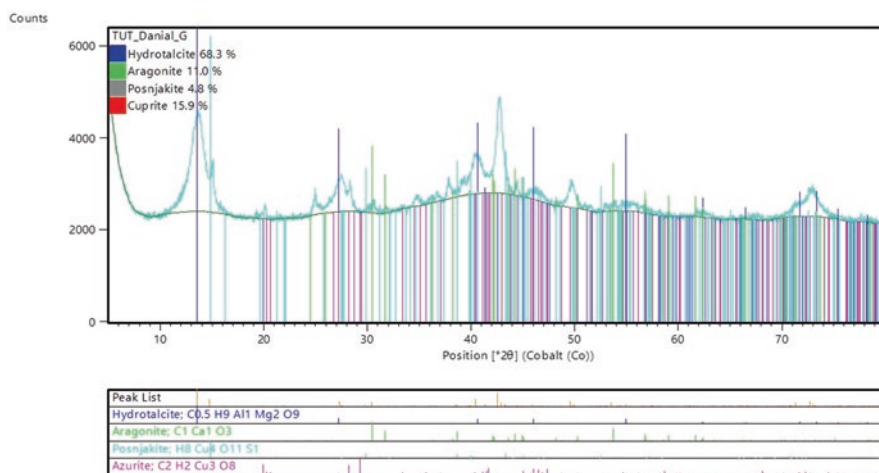

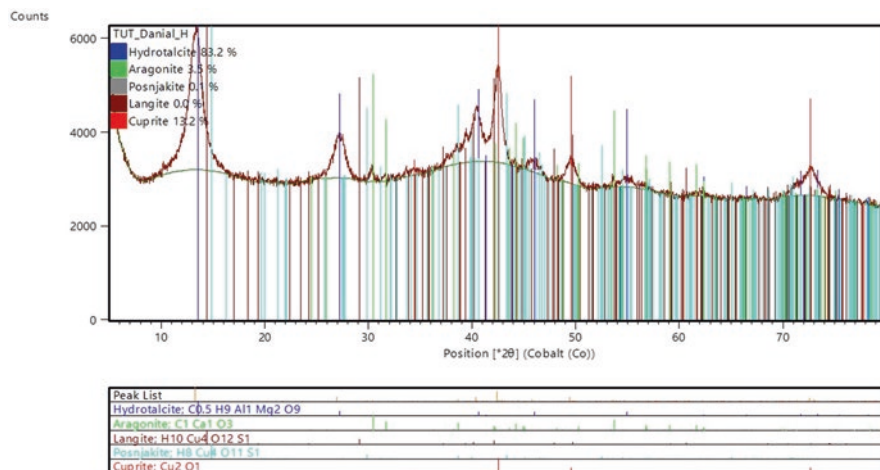**Fig. 6.8** XRD result of copper precursor obtained under 85 °C/340 rpm

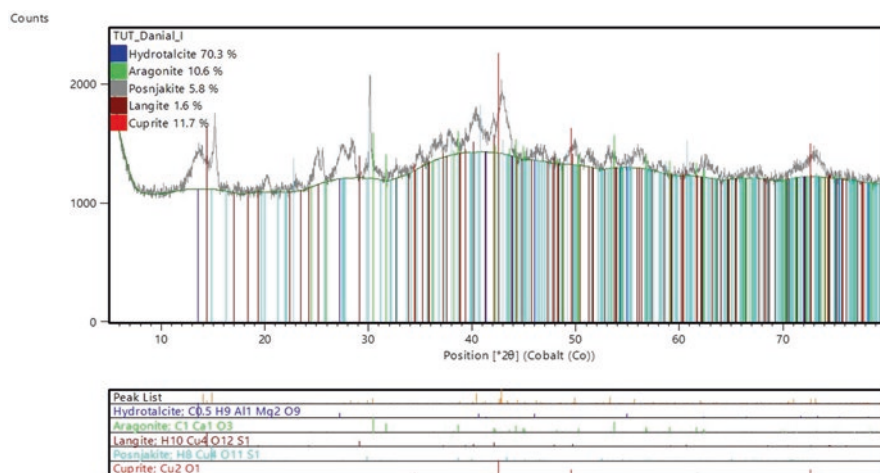**Fig. 6.9** XRD result of copper precursor obtained under 85 °C/740 rpm

Fig. 6.10 XRD result of copper precursor obtained under 85 °C/480 rpm

6.3.1.10 Optimum TC for Production of Copper Precursor

It is shown that the amount of copper-containing compounds (CCC) in the copper precursor obtained from the PPLS of low-grade waste metal dust (i.e. CSD) can be measured accurately by using the TC of temperature and agitation speed (Table 6.2). Based on the results obtained (Table 6.5), the optimum TC that produced the highest CCC (20.7%) is 85 °C/340 rpm (Fig. 6.11).

The variation in percentage contents of hydrotalcite and aragonite in copper precursor can be seen in Table 6.5. Based on the results obtained in Table 7.5, the

highest combination of hydrotalcite (92.3%) and aragonite (2.7%) contents, none-copper-containing compounds is obtained under TC 55 °C/340 rpm (Fig. 6.12) while the least combination of hydrotalcite (68.3%) and aragonite (11.0%) contents is obtained under TC 85 °C/340 rpm (Fig. 6.12); this is consistent with the claim of optimum TC for production copper precursor is 85 °C/340 rpm (Table 6.5).

6.3.2 Mineralogy of Copper Oxide Nanoparticles

The copper precursor that was produced under optimum TC (Table 6.5) was used as the starting material for the production of the copper oxide nanoparticles (CuO-NPs). This copper precursor was subjected to the TC in Table 6.4. The results of the TC are reported in the subsequent part of this paper.

6.3.2.1 Mineralogy of CuO-NPs Produced under 650 °C/1 h

The XRD machine was used to characterize the crystal structure and phase purity of the CuO-NPs generated under TC of 650 °C/1 h (Table 6.4). Figure 6.13 demonstrates that exactly 47.2% of all the diffraction peaks were indexed to tenorite, while 12.5%, 15.4%, 16.0%, 5.4%, and 3.6% of the remaining peaks were indexed to the none-copper-containing compounds, which are magnetite, sodium aluminium phosphate, disodium calcium silicate, grossular ferrian, periclase, respectively.

Table 6.5 Percentage mineralogical composition of copper precursor

TC	Mineralogy of copper precursor					
	Hydrotalcite (%)	Aragonite (%)	Copper-containing compounds			TCCC (%)
			Posnjakite (%)	Langite (%)	Cuprite (%)	
25 °C/340 rpm	87.1	4.8	0.1	0.0	8.1	8.2
25 °C/740 rpm	82.9	5.0	0.1	0.0	12.1	12.2
25 °C/1480 rpm	86.5	4.5	0.1	0.0	9.0	9.1
55 °C/340 rpm	92.3	2.7	0.0	0.0	5.1	5.1
55 °C/740 rpm	88.1	3.0	0.1	0.0	8.8	8.9
55 °C/1480 rpm	89.5	2.6	0.3	0.1	7.5	7.9
85 °C/340 rpm	68.3	11.0	4.8	0.0	15.9	20.7
85 °C/740 rpm	83.2	3.5	0.1	0.0	13.2	13.2
85 °C/1480 rpm	70.3	10.6	5.8	1.6	11.7	19.1

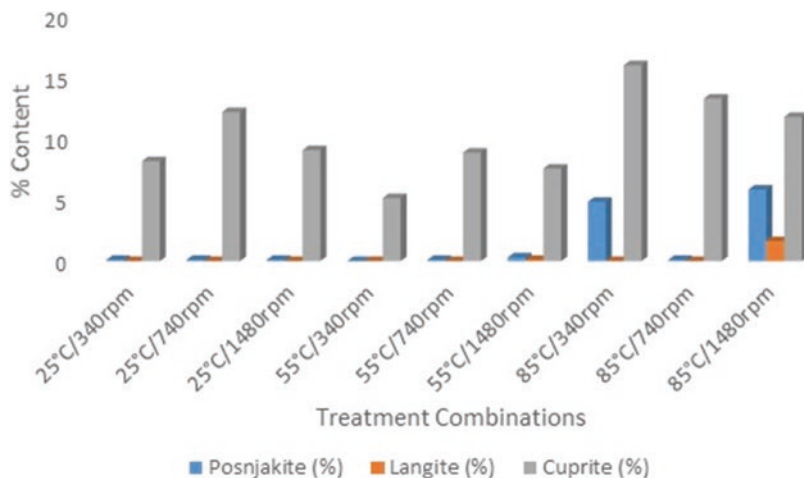Key: TCCC = Total copper-containing compounds

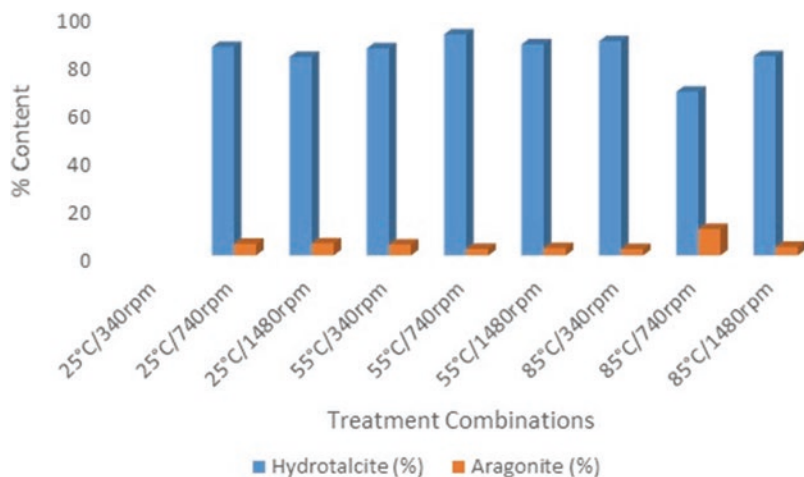**Fig. 6.11** Percentage content of copper-containing compounds in copper precursor at different TC

Fig. 6.12 Percentage content of hydrotalcite and aragonite in copper precursor at different TC

6.3.2.2   Mineralogy of CuO-NPs Produced under 650 °C/2 h

The CuO-NPs produced under TC of 650 °C/2 h (Table 6.4) were characterized in terms of their crystal structure and phase purity using an XRD machine. Figure 6.14 shows that exactly 46.7% of all the diffraction peaks were indexed to tenorite, while the remaining peaks were indexed to the non-copper-containing substances, such as magnetite, sodium aluminium phosphate, disodium calcium silicate, grossular ferrian, and periclase, at rates of 14.0%, 15.8%, 11.6%, 8.1%, and 3.8%, respectively.
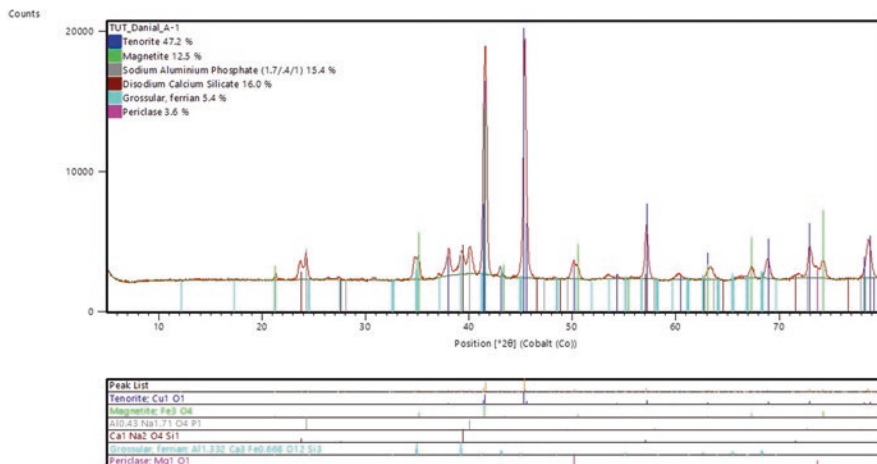
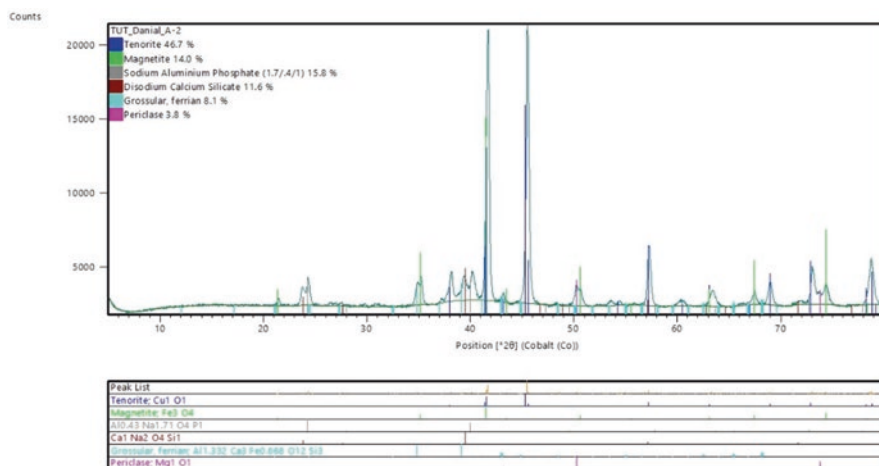**Fig. 6.13** XRD result of CuO-NPs obtained under 650 °C/1 h

Fig. 6.14 XRD result of CuO-NPs obtained under 650 °C/2 h

6.3.2.3 Mineralogy of CuO-NPs Produced under 650 °C/3 h

Using the XRD machine, the CuO-NPs produced at TC of 650 °C/3 h (Table 7.4) were examined for their crystal structure and phase purity. Figure 6.15 demonstrates that exactly 50.1% of all the diffraction peaks were indexed to tenorite, while the remaining peaks were indexed, at percentages of 12.8%, 14.9%, 13.1%, 5.4%, and 3.8%, to the non-copper-containing materials, such as magnetite, sodium aluminium phosphate, disodium calcium silicate, grossular ferrian, and periclase, respectively.

6.3.2.4   Mineralogy of CuO-NPs Produced Under 750 °C/1 h

CuO-NPs generated at TC of 750 °C/1 h (Table 7.4) were subjected to XRD analysis to determine the crystal structure and phase purity. Figure 6.16 shows that exactly 48.7% of all the diffraction peaks were indexed to tenorite, while the remaining peaks were indexed to non-copper-containing compounds like magnetite, sodium aluminium phosphate, disodium calcium silicate, grossular ferrian, and periclase at percentages of 8.8%, 13.0%, 17.5%, 8.6%, and 3.4%, respectively.

6.3.2.5   Mineralogy of CuO-NPs Produced Under 750 °C/2 h

To ascertain the crystal structure and phase purity of CuO-NPs produced at TC of 750 °C/2 h (Table 6.4), XRD analysis was performed. Figure 6.17 demonstrates that exactly 51.3% of all diffraction peaks were assigned to tenorite, while the remaining peaks were assigned to non-copper-containing substances like magnetite, sodium aluminium phosphate, disodium calcium silicate, grossular ferrian, and periclase at percentages of 12.0%, 17.8%, 10.1%, 6.0%, and 2.7%, respectively.

6.3.2.6   Mineralogy of CuO-NPs Produced Under 750 °C/3 h

XRD examination was done to determine the crystal structure and phase purity of CuO-NPs produced at a TC of 750 °C/3 h (Table 6.4). According to Fig. 6.18, tenorite accounted for exactly 50.8% of all diffraction peaks, with the remaining peaks being assigned to non-copper-containing materials like magnetite, sodium aluminium phosphate, disodium calcium silicate, grossular ferrian, and periclase at percentages of 11.1%, 16.8%, 13.2%, 6.2%, and 1.9%, respectively.
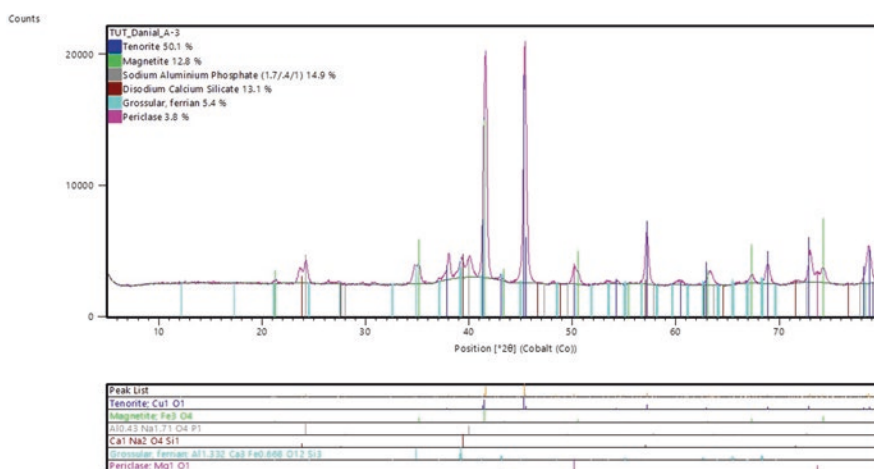

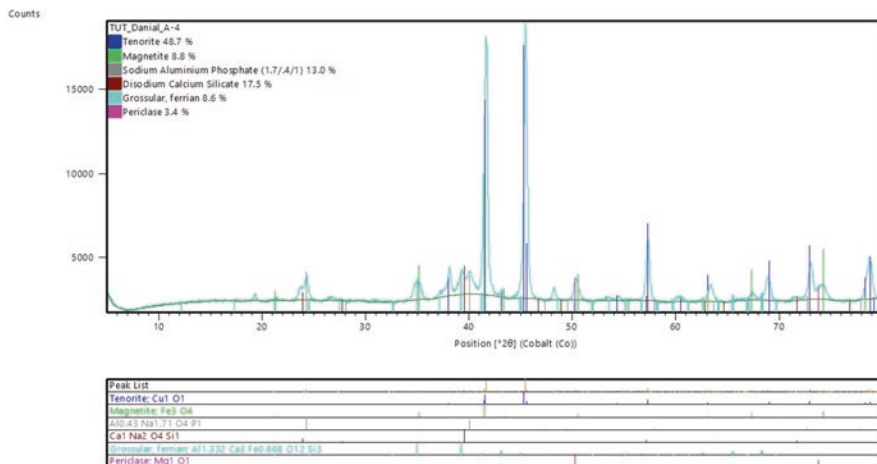**Fig. 6.15**   XRD result of CuO-NPs obtained under 650 °C/3 h

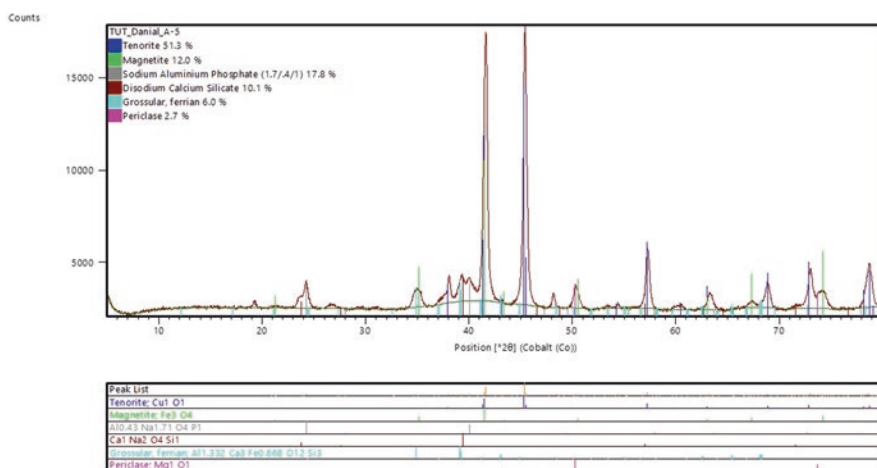**Fig. 6.16** XRD result of CuO-NPs obtained under 750 °C/1 h

Fig. 6.17 XRD result of CuO-NPs obtained under 750 °C/2 h

6.3.2.7 Mineralogy of CuO-NPs Produced Under 850 °C/1 h

CuO-NPs generated at a TC of 850 °C/1 h (Table 6.4) were subjected to an XRD investigation to ascertain their crystal structure and phase purity. Tenorite accounted for exactly 51.3% of all diffraction peaks. The remaining peaks were ascribed to non-copper-containing substances such as magnetite, sodium aluminium phosphate, disodium calcium silicate, and grossular ferrian, at percentages of 14.4%, 17.7%, 11.4%, and 5.2%, respectively. These are all shown in Fig. 6.19.
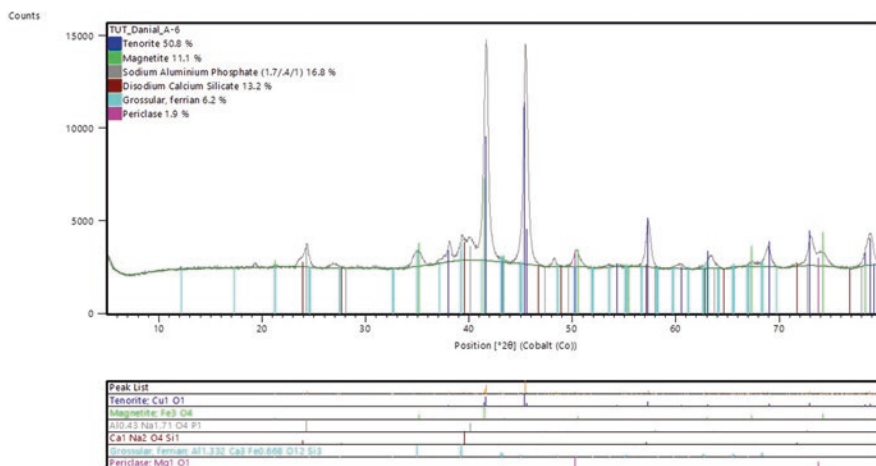
Fig. 6.18   XRD result of CuO-NPs obtained under 750 °C/3 h

6.3.2.8   Mineralogy of CuO-NPs Produced Under 850 °C/2 h

An XRD analysis was performed on CuO-NPs produced at a TC of 850 °C/2 h
(Table 6.4) to determine their crystal structure and phase purity. Exactly 48.9% of
all diffraction peaks were accounted for by tenorite. The remaining peaks, with
percentages of 15.9%, 14.9%, 14.4%, and 5.9%, were attributed to non-copper-
containing materials such as magnetite, sodium aluminium phosphate, disodium
calcium silicate, and grossular ferrian. All of these are displayed in Fig. 6.20.

6.3.2.9   Mineralogy of CuO-NPs Produced Under 850 °C/3 h

CuO-NPs produced at a TC of 850 °C/3 h (Table 6.4) were subjected to an XRD
investigation to ascertain their crystal structure and phase purity. Tenorite accounted
for exactly 47.0% of all diffraction peaks. Non-copper-containing substances
including magnetite, sodium aluminium phosphate, disodium calcium silicate, and
grossular ferrian were blamed for the remaining peaks, which had percentages of
16.8%, 10.9%, 17.9%, and 7.5%. These are all shown in Fig. 6.21.

6.3.2.10   Optimum TC for Production of CuO-NPs

It is shown that the amount of copper compound (CC) in the CuO-NPs obtained
from the copper precursor produced from the WCD can be measured accurately by
using the TC of temperature and agitation speed (Table 6.4). Based on the results
obtained (Table 6.6), the optimum TC that produced the highest CC (51.3%) is
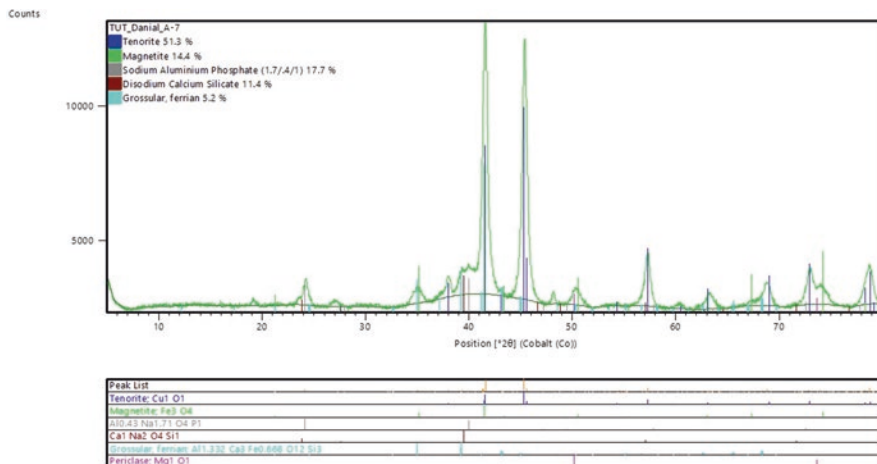750 °C/2 h (Fig. 6.22).

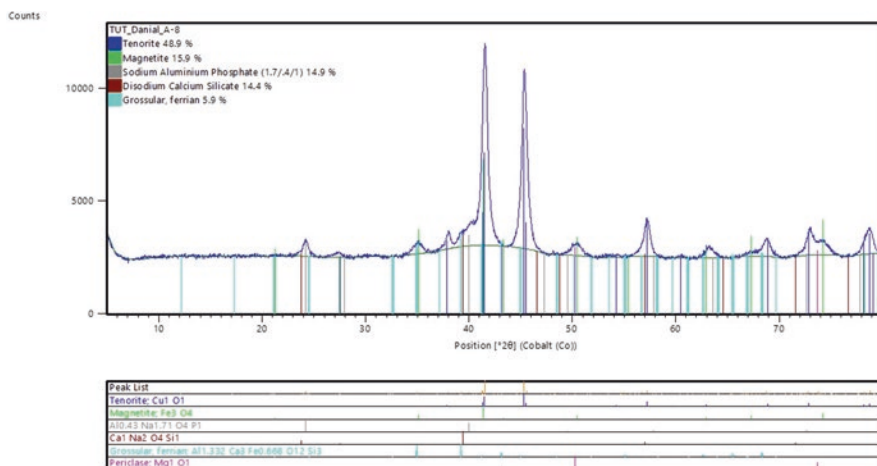**Fig. 6.19** XRD result of CuO-NPs obtained under 850 °C/1 h

Fig. 6.20 XRD result of CuO-NPs obtained under 850 °C/2 h

The variation in percentage contents of magnetite, sodium aluminium phosphate, disodium calcium silicate, grossular ferrian, and periclase in CuO-NPs can be seen in Table 6.6. Based on the results obtained in Table 6.6, the highest combination of magnetite (14.0%), sodium aluminium phosphate (15.8%), disodium calcium silicate (11.6%), grossular ferrian (8.1%), and periclase (3.8%), none-copper-containing compounds (NCCC) is obtained under TC 650 °C/2 h (Fig. 6.23) while the least combination of magnetite (12.0%), sodium aluminium phosphate (17.8%), disodium calcium silicate (10.1%), grossular ferrian (6.0%), and periclase (2.7%) contents is obtained under TC 750 °C/2 h (Fig. 6.23); this is consistent with the claim of optimum TC for production Cu-NPs is 750 °C/2 h (Table 6.6).
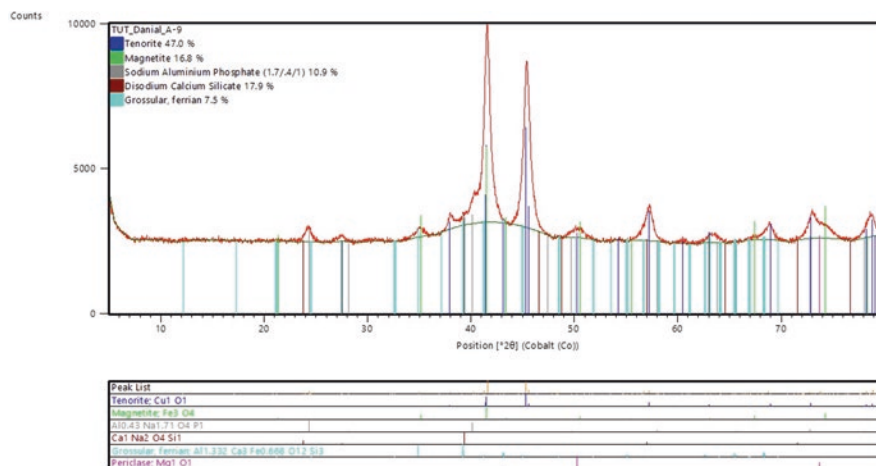
Fig. 6.21 XRD result of CuO-NPs obtained under 850 °C/3 h

Table 6.6 Summary of mineralogical composition of CuO-NPs at different TC

TC	Mineralogical composition of CuO-NPs						Total NCCC (%)
	Tenorite (%)	None-copper-containing compounds (NCCC)					
		Magnetite (%)	Sodium aluminium phosphate (%)	Disodium calcium silicate (%)	Grossular ferrian (%)	Periclase (%)	
650 °C/1 h	47.2	12.5	15.4	16.0	5.4	3.6	52.9
650 °C/2 h	46.7	14.0	15.8	11.6	8.1	3.8	53.3
650 °C/3 h	50.1	12.8	14.9	13.1	5.4	3.8	50.0
750 °C/1 h	48.7	8.8	13.0	17.5	8.6	3.4	51.3
750 °C/2 h	51.3	12.0	17.8	10.1	6.0	2.7	48.6
750 °C/3 h	50.8	11.1	16.8	13.2	6.2	1.9	48.2
850 °C/1 h	51.3	14.4	17.7	11.4	5.2	0.0	48.7
850 °C/2 h	48.9	15.9	14.9	14.4	5.9	0.0	51.1
850 °C/3 h	47.0	16.8	10.9	17.9	7.5	0.0	53.1

6.3.3   Characterization of CuO-NPs

6.3.3.1   SEM

The morphology of the CuO-NPs powder was examined using the SEM machine (Fig. 6.24). The SEM images indicate that the particles are flower like in shape. Temperature is observed to play an important part in the morphology of the developed CuO-NPs, presupposing that the shape of the CuO-NPs can be tuned by changing the temperature.
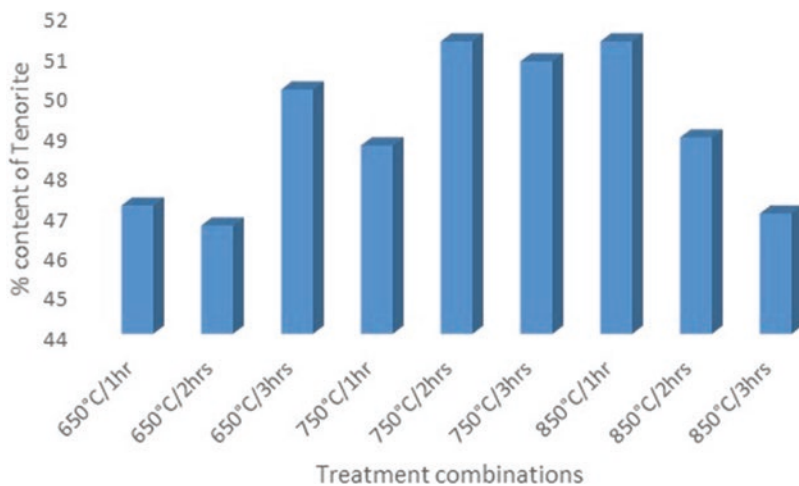
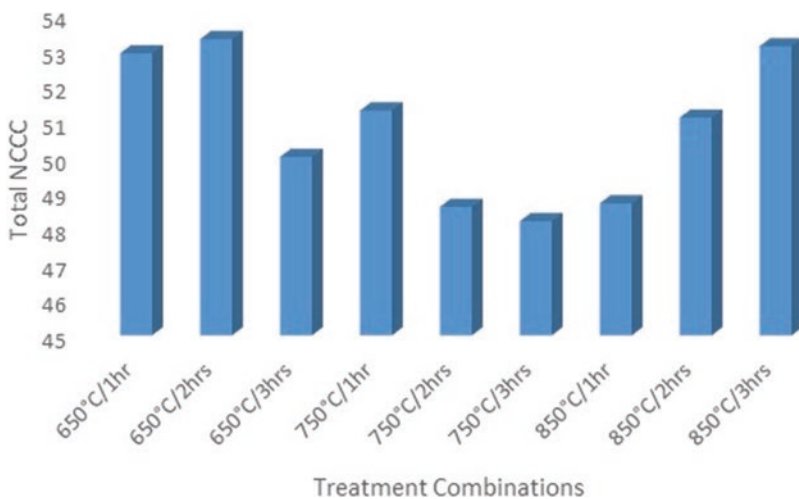**Fig. 6.22** Percentage content of CC in CuO-NPs at different TC

Fig. 6.23 Percentage content of NCCC in CuO-NPs at different TC

6.3.3.2 TEM

The TEM images in Fig. 6.25 show no specific defect and average crystallite size is estimated as 35 ± 5 nm. The TEM images indicate that the particles are cube like in shape.

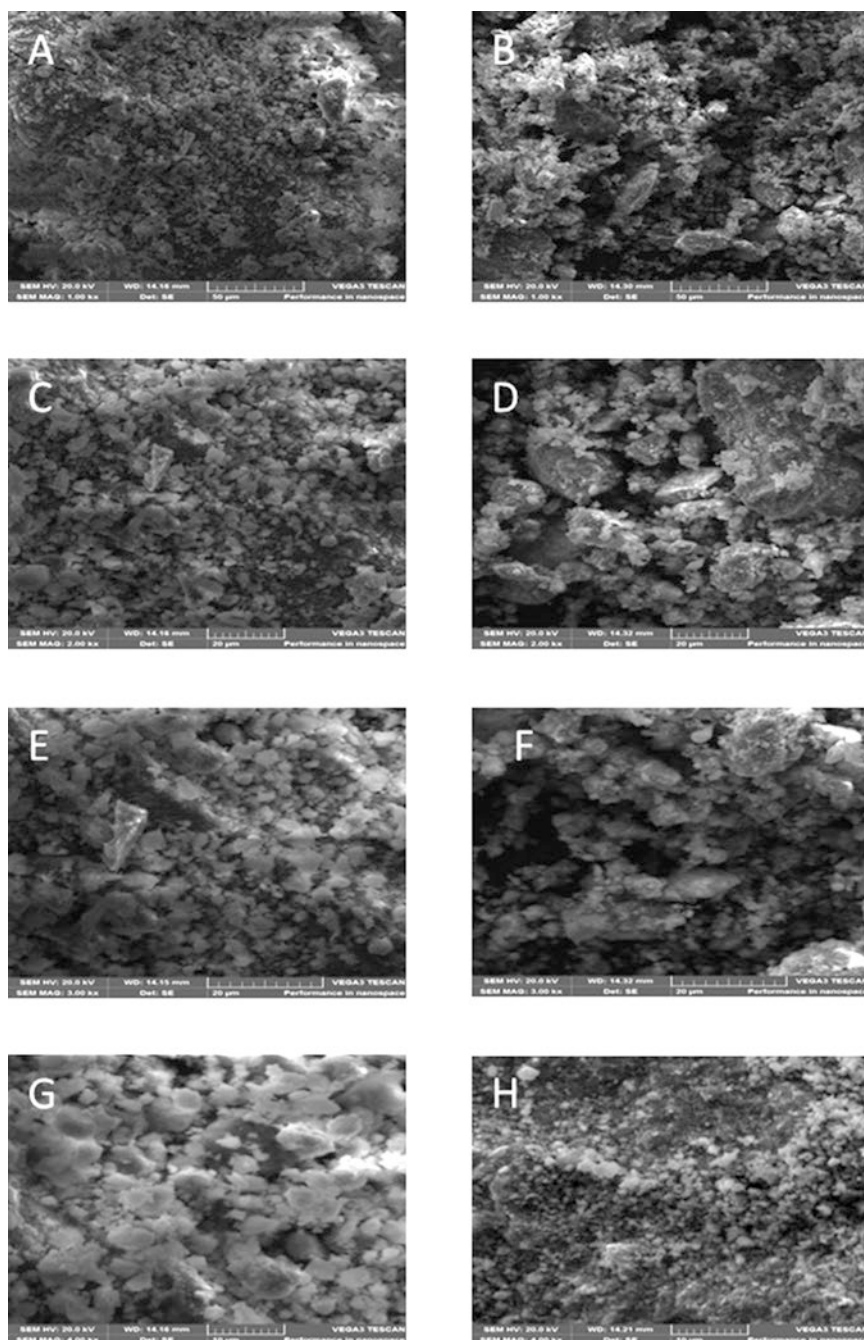**Fig. 6.24** SEM images showing the flower like shape of developed CuO-NPs observed under (**a** and **b**) 10, 000x, (**c** and **d**) 20,000×, (**e** and **f**) 30,000×, and (**g** and **h**) 40,000× magnifications
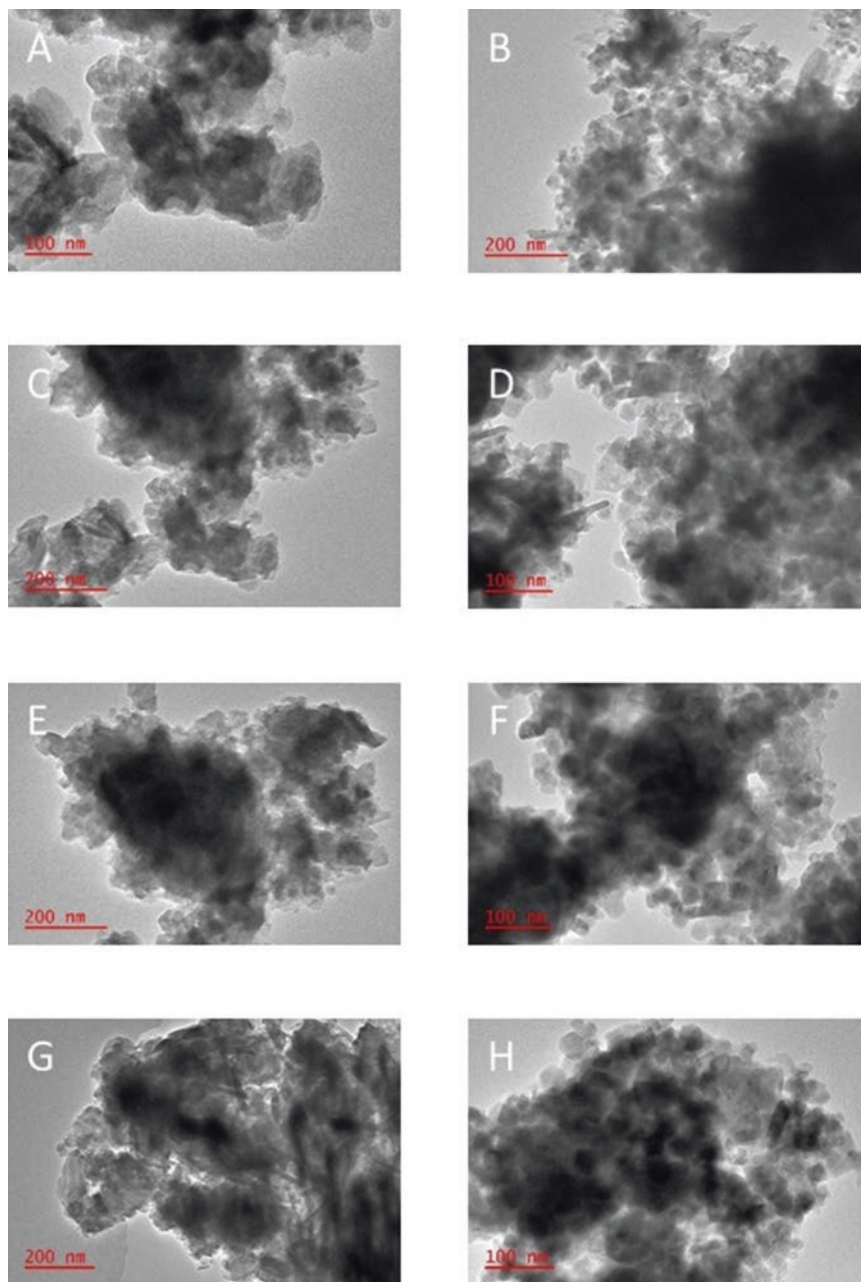
Fig. 6.25 TEM images of the CuO-NPs [A-H], produced from WCD

6.4 Conclusions

The aim of the study was to develop CuO-NPs from leach solution of low-grade WCD. Several deductions were reached in the course of this study. Amongst these deductions are the following:

1. The optimum TC that produced the highest copper-containing compounds in the copper precursor (20.7%) is 85 °C/340 rpm.
2. The optimum TC that produced the highest copper compound in the CuO-NPs (51.3%) is 750 °C/2 h.
3. Angulars to spherical CuO-NPs were successfully prepared by thermal decomposition method with mean diameter of 35 ± 5 nm.

These results represent a trend towards optimum experimental conditions aimed at maximizing CuO-NPs output and minimizing contaminants. It can be concluded that since this method does not require organic solvents, expensive raw materials, and complicated equipment, it is superior to the other methods for the synthesis of CuO-NPs from leach solution (i.e. $CuSO_4$ solution) of low-grade WCD.

References

1. D.O. Okanigbe, A.P.I. Popoola, A.A. Adeleke, Characterization of copper smelter dust for copper recovery. Procedia Manuf. **7**, 121–126 (2017)
2. X. Zhang, D. Zhang, X. Ni, J. Song, H. Zheng, Synthesis and electrochemical properties of different sizes of the CuO particles. J. Nanopart. Res. **10**(5), 839–844 (2008)
3. M.A. Rafea, N. Roushdy, Determination of the optical band gap for amorphous and nanocrystalline copper oxide thin films prepared by SILAR technique. J. Phys. D. Appl. Phys. **42**(1), 015413 (2008)
4. T. Kida, T. Oka, M. Nagano, Y. Ishiwata, X.G. Zheng, Synthesis and application of stable copper oxide nanoparticle suspensions for nanoparticulate film fabrication. J. Am. Ceram. Soc. **90**(1), 107–110 (2007)
5. N. Topnani, S. Kushwaha, T. Athar, Wet synthesis of copper oxide nanopowder. Int. J. Green Nanotechnol. Mater. Sci. Eng. **1**(2), M67–M73 (2010)
6. M.A. Dar, Y.S. Kim, W.B. Kim, J.M. Sohn, H.S. Shin, Structural and magnetic properties of CuO nanoneedles synthesized by hydrothermal method. Appl. Surf. Sci. **254**(22), 7477–7481 (2008)
7. J. Wang, S. He, Z. Li, X. Jing, M. Zhang, Synthesis of claw-like CuO and its catalytic activity in the thermal decomposition of ammonium perchlorate. Mater. Sci. Pol. **27**(2), 501–507 (2009)
8. X. Zhang, D. Zhang, X. Ni, H. Zheng, Optical and electrochemical properties of nanosized CuO via thermal decomposition of copper oxalate. Solid State Electron. **52**(2), 245–248 (2008)
9. C. Li, Y. Yin, H. Hou, N. Fan, F. Yuan, Y. Shi, Q. Meng, Preparation and characterization of Cu(OH)2 and CuO nanowires by the coupling route of microemulsion with homogenous precipitation. Solid State Commun. **150**(13–14), 585–589 (2010)

10. B.J. Hansen, N. Kouklin, G. Lu, I.K. Lin, J. Chen, X. Zhang, Transport, analyte detection, and opto-electronic response of p-type CuO nanowires. J. Phys. Chem. C **114**(6), 2440–2447 (2010)
11. C.T. Hsieh, J.M. Chen, H.H. Lin, H.C. Shih, Field emission from various CuO nanostructures. Appl. Phys. Lett. **83**(16), 3383–3385 (2003)
12. C.C. Li, M.H. Chang, Colloidal stability of CuO nanoparticles in alkanes via oleate modifications. Mater. Lett. **58**(30), 3903–3907 (2004)
13. M.H. Chang, H.S. Liu, C.Y. Tai, Preparation of copper oxide nanoparticles and its application in nanofluid. Powder Technol. **207**(1–3), 378–386 (2011)
14. S. Anandan, X. Wen, S. Yang, Room temperature growth of CuO nanorod arrays on copper and their application as a cathode in dye-sensitized solar cells. Mater. Chem. Phys. **93**(1), 35–40 (2005)
15. X.P. Gao, J.L. Bao, G.L. Pan, H.Y. Zhu, P.X. Huang, F. Wu, D.Y. Song, Preparation and electrochemical performance of polycrystalline and single crystalline CuO nanorods as anode materials for Li ion battery. J. Phys. Chem. B **108**(18), 5547–5551 (2004)
16. C.L. Carnes, K.J. Klabunde, The catalytic methanol synthesis over nanoparticle metal oxide catalysts. J. Mol. Catal. A Chem. **194**(1–2), 227–236 (2003)
17. Y. Kobayashi, T. Maeda, K. Watanabe, K. Ihara, Y. Yasuda, T. Morita, Preparation of CuO nanoparticles by metal salt-base reaction in aqueous solution and their metallic bonding property. J. Nanopart. Res. **13**(10), 5365–5372 (2011)
18. L. Sun, Z. Zhang, Z. Wang, Z. Wu, H. Dang, Synthesis and characterization of CuO nanoparticles from liquid ammonia. Mater. Res. Bull. **40**(6), 1024–1027 (2005)
19. P.J. Cai, M. Shi, Large scale synthesis of shuttle like CuO nanocrystals by microwave irradiation, in *Advanced Materials Research*, vol. 92, (Trans Tech Publications Ltd., 2010), pp. 117–123
20. D. Han, H. Yang, C. Zhu, F. Wang, Controlled synthesis of CuO nanoparticles using Triton X-100-based water-in-oil reverse micelles. Powder Technol. **185**(3), 286–290 (2008)
21. R. Ranjbar-Karimi, A. Bazmandegan-Shamili, A. Aslani, K. Kaviani, Sonochemical synthesis, characterization and thermal and optical analysis of CuO nanoparticles. Phys. B Condens. Matter **405**(15), 3096–3100 (2010)
22. N. Liu, D. Wu, H. Wu, C. Liu, F. Luo, A versatile and "green" electrochemical method for synthesis of copper and other transition metal oxide and hydroxide nanostructures. Mater. Chem. Phys. **107**(2–3), 511–517 (2008)
23. Q. Liu, H. Liu, Y. Liang, Z. Xu, G. Yin, Large-scale synthesis of single-crystalline CuO nanoplatelets by a hydrothermal process. Mater. Res. Bull. **41**(4), 697–702 (2006)
24. W. Jia, E. Reitz, P. Shimpi, E.G. Rodriguez, P.X. Gao, Y. Lei, Spherical CuO synthesized by a simple hydrothermal reaction: Concentration-dependent size and its electrocatalytic application. Mater. Res. Bull. **44**(8), 1681–1686 (2009)
25. W. Jisen, Y. Jinkai, S. Jinquan, B. Ying, Synthesis of copper oxide nanomaterials and the growth mechanism of copper oxide nanorods. Mater. Des. **25**(7), 625–629 (2004)
26. W. Wang, Y. Zhan, X. Wang, Y. Liu, C. Zheng, G. Wang, Synthesis and characterization of CuO nanowhiskers by a novel one-step, solid-state reaction in the presence of a nonionic surfactant. Mater. Res. Bull. **37**(6), 1093–1100 (2002)
27. F. Bakhtiari, Synthesis and characterization of tenorite (CuO) nanoparticles from smelting furnace dust (SFD). J. Min. Metall. B Metall. **49**(1), 21–21 (2013)
28. J. Zhu, D. Li, H. Chen, X. Yang, L. Lu, X. Wang, Highly dispersed CuO nanoparticles prepared by a novel quick-precipitation method. Mater. Lett. **58**(26), 3324–3327 (2004)
29. R. Wu, Z. Ma, Z. Gu, Y. Yang, Preparation and characterization of CuO nanoparticles with different morphology through a simple quick-precipitation method in DMAC–water mixed solvent. J. Alloys Compd. **504**(1), 45–49 (2010)
30. R. Ahmadi, M.H. Hosseini, A. Masoudi, Avrami behavior of magnetite nanoparticles formation in co-precipitation process. J. Min. Metall. B Metall. **47**(2), 211–218 (2011)
31. H. Fan, L. Yang, W. Hua, X. Wu, Z. Wu, S. Xie, B. Zou, Controlled synthesis of monodispersed CuO nanocrystals. Nanotechnology **15**(1), 37 (2003)

32. F. Bakhtiari, E. Darezereshki, One-step synthesis of tenorite (CuO) nano-particles from Cu4(SO4)(OH)6 by direct thermal-decomposition method. Mater. Lett. **65**(2), 171–174 (2011)

33. S. Thimmaiah, M. Rajamathi, N. Singh, P. Bera, F. Meldrum, N. Chandrasekhar, R. Seshadri, A solvothermal route to capped nanoparticles of γ-Fe2O3 and CoFe2O4. J. Mater. Chem. **11**(12), 3215–3221 (2001)

34. J. Yang, G.H. Cheng, J.H. Zeng, S.H. Yu, X.M. Liu, Y.T. Qian, Shape control and characterization of transition metal diselenides MSe2 (M=Ni, Co, Fe) prepared by a solvothermal-reduction process. Chem. Mater. **13**(3), 848–853 (2001)

35. K. Byrappa, M. Yoshimura, *Handbook of Hydrothermal Technology* (William Andrew, 2012)

36. A. Umer, S. Naveed, N. Ramzan, M.S. Rafique, Selection of a suitable method for the synthesis of copper nanoparticles. Nano **7**(05), 1230005 (2012)

37. K. Byrappa, Growth of quartz crystals, in *Bulk Crystal Growth of Electronic, Optical and Optoelectronic Materials*, (Wiley, 2005), pp. 387–406

38. E. Darezereshki, F. Bakhtiari, A novel technique to synthesis of tenorite (CuO) nanoparticles from low concentration CuSO4 solution. J. Min. Metall. B Metall. **47**(1), 73–78 (2011)

39. D.O. Okanigbe, Production of copper and copper oxide nano-particles from leach solution of low grade copper smelter dust. Thesis, Dissertation, 2019.

40. S. Makaka, M. Aziz, A. Nesbitt, Copper recovery in a bench-scale carrier facilitated tubular supported liquid membrane system. J. Min. Metall. B Metall. **46**, 67 (2010)

41. N. Koga, J.M. Criado, H. Tanaka, Reaction pathway and kinetics of the thermal decomposition of synthetic brochantite. J. Therm. Anal. Calorim. **49**(3), 1467–1475 (1997)